PAPER

Lifetime based axial contrast enable simple 3D-STED imaging

Methods and Applications in Fluorescence

PAPER

Lifetime based axial contrast enable simple 3D-STED imaging

Yuanqing Ma[1,2,3,*], **Alex Macmillan**[4], **Ying Yang**[5] **and Katharina Gaus**[1,†]

[1] EMBL Australia Node in Single Molecule Science, and ARC Centre of Excellence in Advanced Molecular Imaging School of Medical Sciences, The University of New South Wales, 2052 Sydney, Australia
[2] The Garvan Institute of Medical Research, St Vincent's Clinical School, Faculty of Medicine, UNSW Sydney, Sydney, NSW 2010, Australia
[3] ACRF Centre for Intravital Imaging of Niches for Cancer Immune Therapy (INCITe), Sydney, NSW 2010, Australia
[4] Katharina Gaus Light Microscopy Facility, University of New South Wales, Kensington, NSW, 2052, Australia
[5] School of Chemistry, Australian Centre for NanoMedicine, and ARC Centre of Excellence in Convergent Bio-Nano Science and Technology, University of New South Wales, Sydney 2052, Australia
[*] Author to whom any correspondence should be addressed.
[†] Deceased

E-mail: mayuanqing8@gmail.com

RECEIVED
14 January 2022

REVISED
27 February 2022

ACCEPTED FOR PUBLICATION
15 March 2022

PUBLISHED
25 March 2022

Keywords: 3D-STED, MIET, Lifetime contrast

Supplementary material for this article is available online

Abstract

Stimulated Emission Depletion (STED) microscopy increase spatial image resolution by laterally sharpening the illumination profile of the confocal microscope. However, it remains compromised in axial resolution. To improve axial STED resolution, constructive interference of the STED depletion beam must be formed surrounding the focal plane to turn off the fluorophores beyond the focal plane. For isotropic 3D-STED resolution, this axial STED interference pattern must be overlayed with the doughnut STED beam at nanometer accuracy. Such optical configurations can be challenging in alignment. In this current work, we introduced a straightforward lifetime based axial contrast in STED microscope by imaging the samples on an ITO coated glass coverslip. The STED laser generates surface plasmon resonance on the ITO surface that enhanced the metal induced energy transfer MIET effect on the ITO surface. The enhanced MIET effect established a lifetime gradient with ~20% dynamic range that extend for mor than 400 nm from the ITO surface. The axial contrast based on the lifetime gradient was directly used for 3D-STED imaging of tubulin fibers inside COS-7 cells, where the vertical displacement of single tubulin fiber was revealed. Lifetime gating could be applied to further improve lateral spatial resolution. Considering that most common implementation of STED microscopes uses pulsed lasers and timing electronics, there is no optical modification of the microscope is required in the current 3D-STED approach.

1. Introduction

Due to the diffraction of light, the diameter of the focused light in the standard laser scanning confocal microscope cannot be finer than 200 nm for the visible light spectrum [1]. Features that dwell within the laser spot cannot be separated as all the fluorophores within the focal spot are excited simultaneously. The STED microscope breaks the diffraction barrier by sharpening the effective point spread function (PSF) of the excitation laser [2]. This is done by introducing a second doughnut-shaped depletion beam which overlays with the excitation laser to turn off the fluorophores in the peripheral region of the focal point. Only the fluorophores located in the exact center of the doughnut beam remain 'on'. A 0–2π vortex helical shaped phase plate is inserted in the STED beam path to alter the wavefront of the STED beam so that it generates a destructive interference pattern at the geometrical center of the focal point and a constructive interference pattern at the peripheral ring [3]. This produces an open-ended tube-like three-dimensional geometry of the STED depletion beam with zero intensity along the z axis. The resulting effective PSF of the STED microscope is like a thin needle. Due to the lack of depletion in the z direction,

there is little resolution enhancement along the axial axis. Although a resolution close to 30 nm can be achieved in XY with STED, the z direction is still limited in the range of ∼1 um [4]. Several approaches have been proposed to increase the resolution in the axial dimension. One method is to combine STED and 4Pi microscope modalities. That is, a coherent STED light source is split into two separate light paths and guided to the same focal point from two opposing objectives. The two beams forms a sharp interference pattern along the *z* axis [5]. By tuning the polarization state of one laser beam, destructive interference with zero intensity can be shifted to the shared focal plane of the two objectives, while constructive interference formed surrounding the focal plane to turn the fluorophores off. For optimized improvement in resolution in both the XY and Z direction, this axial interference pattern must be perfectly superimposed with the doughnut beam to form a sphere-shaped hollow depletion pattern. Isotropic 40 nm 3D resolution has been demonstrated using this configuration [5]. However, the two objective 4pi configuration is cumbersome for sample accessibility and requires additional adjustment of sample buffer composition to reduce local refractive index mismatch [5]. Alternatively, one single objective-based 3D-STED approach has also been proposed, where a similar axial interference pattern with zero intensity at the focal plane is generated from a separate top-hat phase plate. It overlays with the XY doughnut beam at the same focal point to achieve isotropic 3D-STED resolution [6–9]. Although the sample space accessibility is improved compared to the 4pi 3D-STED, the setup still requires sophisticated optical configuration and nanometer precision alignment. Optical aberrations have also been reported in these systems which prevent achieving optimal resolution [10, 11]. An alternative simpler hybrid phase plate has been reported that integrates the doughnut and top-hat phase plates effect in a single beam path [4]. However, using this method the resolution was compromised in the XY direction [4].

The recently reported Metal Induced Energy Transfer (MIET) technique has been shown to improve the axial resolution without additional optical modifications of the microscope. The principle of MIET is based on the near field resonance effect that occurs when the fluorophore is placed in close proximity to the metal surface [12]. When the fluorophore is located at close distance <=150 nm to the metal film, the excited energy is transferred to the surface plasmons of the metal surface through near field resonance effect. This induces a reduction of the apparent lifetime of the fluorophore. The resonance effect is reminiscent to the well-known Förster resonance energy transfer (FRET) between two fluorophores [13], while the working distance range for MIET is much longer than FRET. In MIET, the requirement for the acceptor is that it should contain free electrons which are able to resonate with the electromagnetic wave from the excited fluorophores. Due to the substantially large absorption cross-section of the metal film as an acceptor, the resonance effect can be extended linearly for up to 150 nm [14]. As the distance between the fluorophore and metal surface can be deduced from the measured lifetime, MIET has been adopted as an axial super-resolution imaging technique. The achievable z resolution using MIET can be down to ∼5 nm in both point scanning and wide field illumination microscopes [14, 15]. Except the frequently used gold substrate, recently it has been shown that semiconductor materials, such as graphene and indium tin oxide (ITO), can also produce the MIET effect but with shorter axial range of less than 20 nm [16–18]. This is due to the lower abundance of free charge carriers present in the semiconductor to resonate with the electromagnetic field of the dipoles [16]. Nevertheless, one of the drawbacks of imaging through the gold film is the low transmission rate due to the opaque nature of gold. At 10 nm thickness, the transmission efficiency is only ∼10% at 650 nm [19]. In comparison, indium oxide is a highly transparent ceramic semiconductor material. After doping with Tin, it is still highly transparent but more conductive due to increased concentration of free electron carrier [20]. The unique optical and electrical property of ITO has been utilised in many optoelectronic devices, such as solar cells and sensing electrodes [21]. Recently, ITO coated coverslips have also been applied in fluorescence spectroscopy [17, 18]. With a 700 nm thick ITO coating, the transmission efficiency is still greater than 85% in the visible spectrum [22], which makes it highly valuable for photon sensitive super-resolution techniques [23, 24].

The MIET effect generate from the ITO surface is effective for ⩽10 nm distance from the ITO coated surface, which has been used to locate the fluorophores with subnanometer accuracy in the *z* axis [17]. For distance greater than 10 nm, the MIET effect was substantially reduced. However, how will the MIET effect be influenced by the STED laser near the ITO surface is yet unclear. To our knowledge, STED imaging on ITO coated coverslip has not been reported to date. It is known that ITO is transparent to visible light and partially reflective to infrared light due to the plasma frequency of ITO in the infrared spectrums. At plasma frequency, the free electron in ITO become delocalized and oscillates in resonance with the incoming light wave, known as surface plasmon resonance SPR [25, 26]. From nanoantennas single molecule imaging work, it is known that when the dye fluorescence emission band overlays with the locally excited plasmon resonance, reduction of dye lifetime can occur [27]. The plasmon frequency of ITO is blue shifted to the near infrared spectrum with the increase of ITO coating thickness [28]. At 765 nm STED laser wavelength and 750 nm ITO coating thickness that used in current study, we anticipate that the STED

laser could induce SPR on the ITO surface which could potentially enhance the MIET effect. Experimentally, we showed that in presence of the 765 nm STED laser, the MIET effect from the ITO surface was substantially enhanced, which extended for more than 400 nm with more than 20% dynamic range. The effect was not observed on standard glass coverslip or ITO alone. The STED laser enhanced MIET effect generates a steep and long distance range lifetime gradient that was sufficient to detect the axial displacement of single tubulin fibers in COS-7 cells.

2. Result and discussion

2.1 , STED laser enhances the MIET effect of the ITO surface

We anticipate that the MIET effect on the ITO surface can be used to produce axial contrast to the standard STED imaging. Here, we used commercially available ITO coated coverslips with 8-12 Ω electric resistance that are equivalent to 750 nm thickness of ITO coating according to the manufacturer. We acquired STED imaging using the Microtime 200 STED microscope (PicoQuant, GmbH) coupled with a FLIM bee scanner. The sample are excited and depleted by the 40 MHz pulsed 640 nm and 765 nm laser respectively. In the following text, we refer the STED laser as the 765 nm depletion laser and 640 nm laser as the excitation laser. The shape of the STED doughnut was checked by reflection from 100 nm gold nanoparticles. The typical central hollow shaped STED doughnut pattern were confirmed on both the glass substrate and ITO surface (Supplementary figure 1 (available online at stacks.iop.org/MAF/10/035001/mmedia)). We imaged fluorescent polystyrene beads with 430 nm diameter that were labelled with a far-red dye that was suitable for our STED laser light configuration. When imaged at glass surface in absence of STED depletion laser, the dye displayed a single exponential decay with lifetime of 2.3 ns. In presence of STED laser, the dye emission is modified depend on the STED intensity it experiences. At high STED laser intensity, there is high probability for the excited dye to return to ground state through stimulated depletion at the STED laser wavelength. The timing of the depletion laser needs to be adjusted for optimized depletion efficiency [29]. By imaging the beads using the 63X water immersion objective with the STED phase plate removed, we found that having the 765 nm STED depletion laser delayed by 200 ps with respect to the 640 nm excitation laser produced the most efficient dye depletion. The same laser settings were applied for all the following STED image acquisitions. At low STED laser intensity, the STED laser is insufficient to induce simulated depletion. In this case, the STED laser quenches the excited dye lifetime. This is because the STED laser forms an additional decay pathway for the excited fluorophore to return to ground state with an emission of photons in its intrinsic spectrum [6, 30]. The influence of STED laser to the dye lifetime τ can be mathematically described as $\tau = 1/(K_{fl} + \sigma I)$, where, K_{fl} is the intrinsic decay rate, $\sigma$is the absorption cross section of the STED laser, and I is STED laser intensity [31]. Here, we acquired lifetime of a group of randomly selected beads on the glass substrate. We found that as the STED laser intensity increases, the dye lifetime began to decrease at early lifetime bins which formed a noticeable inverted hump on the fluorescence decay at ~1 ns (figure 1(a)). Since a band pass filter (690/70) was placed to reject the STED laser and STED laser stimulated dye emission, we reason the lifetime shortening is due to the insufficient stimulated depletion of the dye. It is noticeable that the decrease of lifetime only occurred for the duration of the STED pulse (figure 1(a)). The lifetime after the STED pulse remained the same as in free space as previously reported [6, 30]. When the pixel lifetime value in the Fast FLIM image that calculated by taking the average photon arrival time of all photons in individual pixels was plotted in histogram, it produced a single peaked gaussian distribution (figure 1(b)). At 17.4 mW STED laser intensity, the lifetime histogram was shift from 2.3 ± 0.4 ns to 1.6 ± 0.4 ns without significant change in the shape of distribution.

In comparison, the lifetime behavior of the dyes on the ITO surface was more complex. We found that the STED laser quenched the dye lifetime at short lifetime time as on the glass substrate, it also enhanced the MIET effect at longer lifetime. At short lifetime scale, the amplitude of the fast decay due to the incomplete STED deletion was substantially increased for the same STED laser intensity on the ITO surface compared to glass substrate as shown in figure 1(c). This is consistent to the previous studies to show that the efficiency of STED depletion was enhanced when the dye was placed inside a metal shell [32, 33]. More interestingly, the dye lifetime decay after the STED pulse was also significantly accelerated on the ITO surface. When the lifetime decay after the STED pulse from 2 ns onward was plotted side by side for the glass substrate and ITO surface under same STED laser intensity (figure 1(c) inset), it was evident that there was an overall faster decay rate on the ITO surface. Suggesting that the overall lifetime decay process of the dye on the ITO surface has been modified. The effect is reminiscent to increased MIET quenching effect as the fluorophores was brought closer the ITO surface as previously reported [17]. This implies the STED laser has enhanced the MIET effect on the ITO surface that potentially due to localized plasmon resonance coupling between the STED laser and ITO surface. The lifetime distribution of average photon arrival time in the Fast FLIM image also showed a more complex nature on the ITO surface. The original peak was shifted from 2.3 ± 0.4 ns to 1.1 ± 0.5 ns, and a second peak at 0.25 ns appeared with increased STED intensity (figure 1(d)). Importantly, we ruled out the possibility

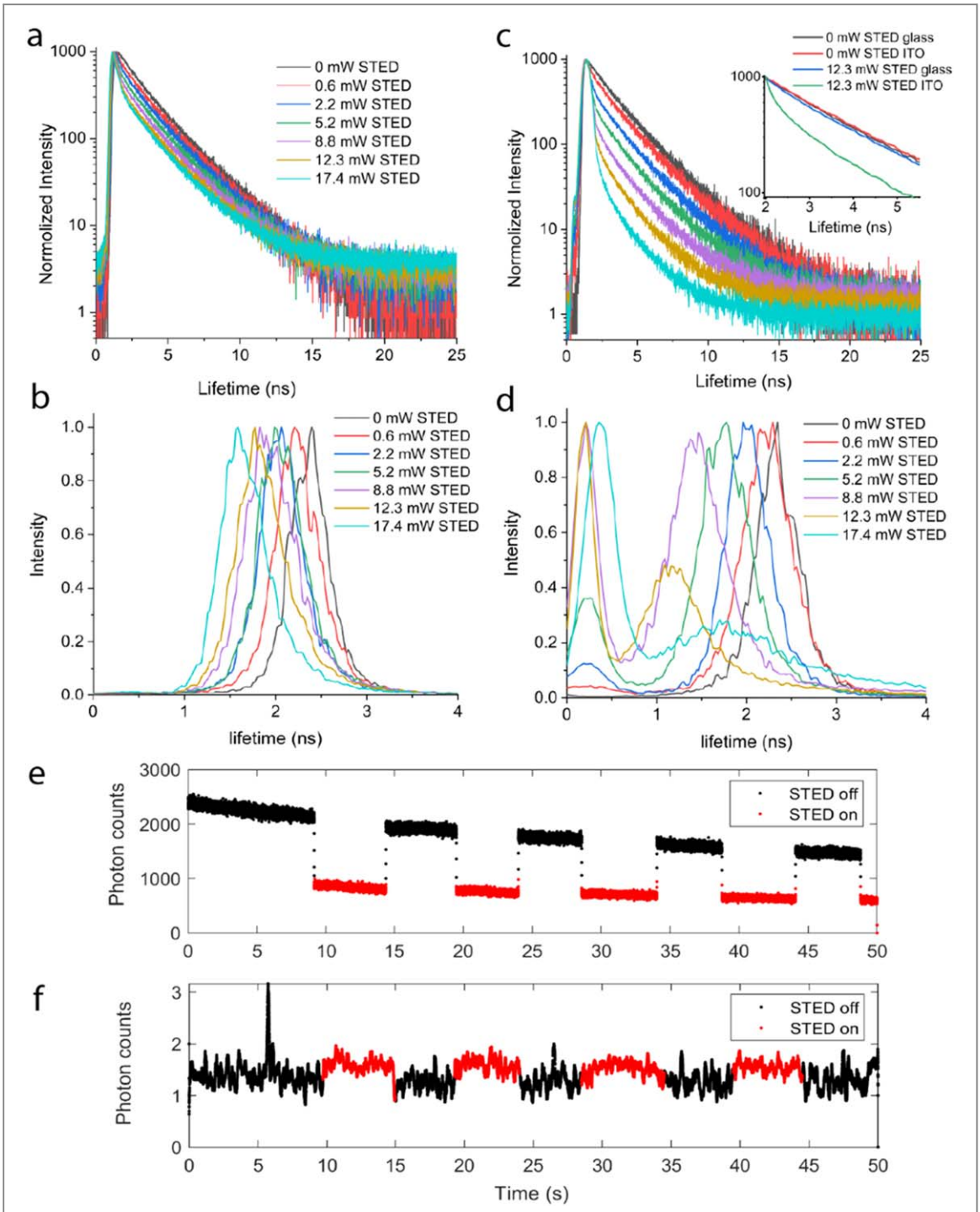

Figure 1. STED Laser enhances MIET effect on the ITO surface. The fluorescence lifetime decay (a), (c) and histogram of pixel lifetime values in the Fast FLIM image (b), (d) of the 430 nm beads on the glass (a), (b) and ITO (c), (d) surfaces at various STED laser power measured at the objective back aperture as indicated. In a and c, the lifetime decay is normalized to 1000 at the peak of the exponential decay. In b and d, the pixel lifetime value in the Fast FLIM is calculated by taking the average photon arrival time in each pixel over the full 25 ns lifetime window, which is equivalent to the center of mass of the lifetime decay. The histogram is normalized to 1 at the gaussian peak. The inset in c showed a cropped lifetime decays between 2 ns to 5.5 ns with and without of 12.3 mW STED on glass and ITO surface as indicated. To ease visual comparison, the decays in the inset were normalized by the lifetime values at 2 ns. (e) and (f), plot of detector intensity by focusing 640 laser on a bead (e) and outside of a bead (f) with STED laser switched off (black) and on (red) intermittently on the ITO surface.

that the fast photons were due to scattering from the 640 nm or STED laser on the ITO surface. Here, we compared the fluorescence intensity emitted from a bead and scattered light outside the bead with constant 640 nm laser illumination while switching the STED laser (8.8 mW) on and off on the ITO surface (figures 1(e), (f)). On the fluorescent bead, the presence of the STED laser depleted the fluorescence by ~60%, without causing notable photobleaching and anti-stoke excitation (figure 1(e)). Outside the beads, the scattered 640 nm laser from the ITO surface was less than 0.1% of the signal from the bead, and the

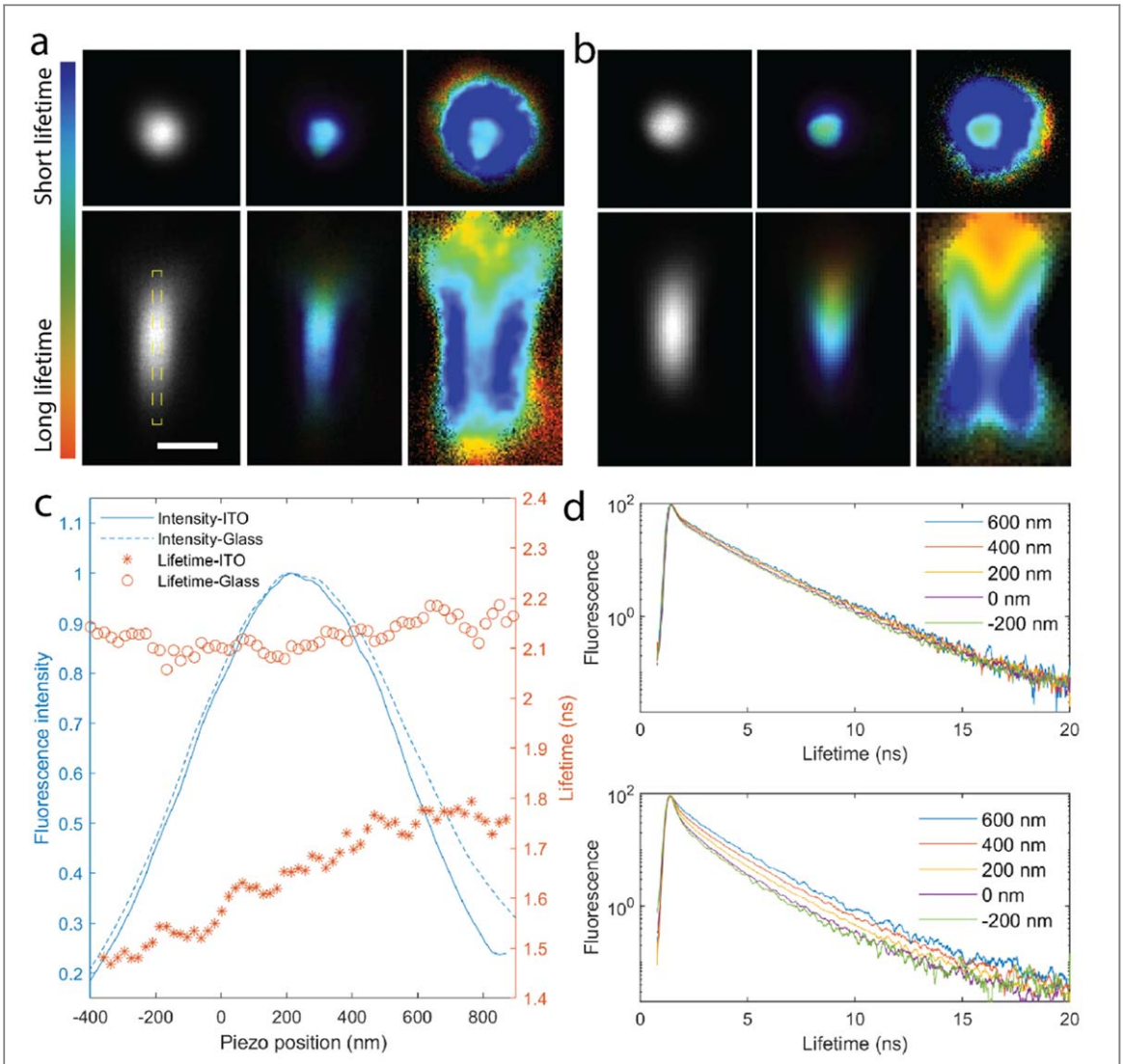

Figure 2. PSF characterization of STED imaging on the ITO surface (a, b) XY and XZ plane image of a single 430 nm bead on glass (a) and ITO coated (b) coverslips. From left to right, the columns are intensity, intensity weighted and non-intensity weighted STED lifetime images, respectively. The lifetime images were color coded from blue to red indicate increase of lifetime. The color scales were optimized independently in a and b to maximize the contrast in display. Scale bar = 500 nm. (c) Plot of the fluorescence intensity (first *Y* axis in blue) and tail fitted lifetime values (second *Y* axis in orange) in the STED doughnut center along the *z* axis of the bead on glass substrate (circle) and ITO surface (stars). A vertical rectangular section in the middle of the XZ image of the bead was selected as indicated by dotted line in a, the horizontal pixels inside the rectangle were binned at each z position to increase photon counts. Here, the extracted lifetime decays at each z position were forced to tail fit to a single exponential model in the range of 2.7 ns to 25 ns to minimize the direct influence from STED laser. The two gaussian curves and corresponding lifetime values were aligned to the center of the beads at the height of 215 nm. (d) Raw lifetime decay profiles at selected piezo positions shown in c on the glass (top) and ITO (bottom) surfaces.

presence of STED laser caused negligible change compared to 640 nm laser alone (figure 1(f)).

2.2 , PSF characterization of STED imaging on the ITO surface

Given the enhanced MIET effect on the ITO surface, we aimed to test whether it could provide a sufficient lifetime gradient along the z direction to introduce axial contrast for 3D-STED imaging. For proper STED imaging, we switched to the 100 × 1.4 Oil objective with the STED plated inserted beneath the objective. Images were acquired in XY and XZ plane of single 430 nm beads on both glass and the ITO coated coverslips. As shown in the XY lifetime image of the bead in figure 2(a) top row 2nd column, the lifetime at the peripheral region of the bead was noticeably shorter compared to the center on the glass substrate. This effect become clearer when the lifetime image was not weighted by photon number as shown in the figure 2(a) top row 3rd column. While the fluorescence is normally well suppressed at the crest of the STED doughnut, dyes that located at the inner circle region between the central intensity zero and doughnut crest can escape complete depletion and emit photons at its intrinsic emission spectrum. Those photons are often short lived due to the influence of STED laser. Similar concentric lifetime patterns of bead have been reported in other STED studies [30, 31]. When the bead was imaged on the ITO surface, a comparable lateral lifetime pattern was

observed but with an overall lifetime shortened compared to the glass substrate (figure 2(b)). Importantly, different lifetime pattern was revealed when the XZ scan of the bead was compared. Here, a rectangular XZ plane across the center of a single bead was scanned with pixel size of 20 nm over the depth of 2 μm. The axial scan was done by the moving the piezo motor attached to the objective. On the glass surface, the lifetime profile in the XZ image was consistent to the XY image, where the lifetime was longer in the center and shorter at the peripheral (figure 2(a) bottom row 2nd and 3rd column) across the entire z axis. There was little lifetime change alone the z direction. On the ITO surface, there was an intense steep lifetime gradient observed alone the z axis. The lifetime was shortest close to the ITO surface and gradually increased as the distance from the ITO surface grew (figure 2(b) bottom row 2nd column). On close inspection of the non-intensity weighted lifetime image (figure 2(b) bottom row 3rd column), it showed that the STED doughnut beam became intensified at the ITO interface. It appeared as a blue triangular cone shaped short lifetime pattern surrounding the central bead. The pattern was laterally extended into the center and covered the bottom section of the bead. The local amplification and longitudinal traveling of the STED laser on the ITO surface implies SPR coupling between the STED laser and ITO coating.

Next, we assessed the axial range of the STED induced MIET effect on the ITO surface. We analyzed the dye lifetime on the XZ image at increasing z position along the bead. To minimize the direct lifetime influence from the STED beam, we selected only a narrow strip of pixels equivalent to 80 nm in width in the middle of the STED doughnut that extend alone the z axis as highlighted by yellow dotted line in figure 2(a). The lifetime decay of the pixels at each z section were binned to increase photon count and tail fitted to a single exponential decay function between 2.7 ns to 25 ns. The fitting was gated from 2.7 ns onward to minimize the direct influence from the STED laser. The results are plotted in figure 2(c), with the overall lifetime of the bead being substantially reduced on the ITO surface, which is consistent to the result acquired in figure 1(d). A gradual increase in lifetime was observed as the distance from the ITO surface increases along the z axis. The lifetime value increased by 20 $\pm$ 3% as the piezo moved up from $-$300 nm to 800 nm relative to the ITO surface. Even at the top of the bead, the lifetime was still substantially lower than the intrinsic lifetime of the dye on glass substrate, suggesting that the STED induced MIET effect likely extends beyond the diameter of the bead in the z direction. In contrast, for the same axial range and image settings, the tail fitted lifetime on the glass substrate has only increased by less than 2.0 $\pm$ 0.3%. A 10-folds increase in lifetime contrast was observed on the ITO coverslip. When the lifetime color scale was adjusted to maximize the contrast (2nd and 3rd columns in 2nd row in figures 2(a) and (b)), greater lifetime contrast along the z axis was clearly observed on the ITO surface. A gradual increase of lifetime was stretched over the entire diameter of the bead from bottom to top. As the displayed lifetime image was smoothed by taking average of neighboring pixels to increase signal to noise ratio (see methods for detail), we also examined the unaveraged raw lifetime decay of piezo positions from 600 nm to $-$200 nm relative to the coverslip as shown in figure 2(d). The gradual decrease of lifetime was evidently visible on the ITO surface, while the lifetime on the glass substrate showed no significant change. In summary, the PSF characterization revealed a sharp lifetime gradient in z axis on the ITO surface with more than 10-folds increase in dynamic range compared to the glass substrate. The lifetime gradient extended over the height of the bead in distance from the ITO surface.

2.3 , 3D-STED lifetime imaging of tubulin filaments in the cell

Given the increased lifetime contrast along the z axis on the ITO surface, we investigated whether the lifetime gradient can be used to produce sufficient axial contrast for 3D-STED imaging of cellular structures inside the cells. For this purpose, we performed STED imaging of tubulin fibers in COS-7 cells. The cells were directly cultured on the ITO surface prior to the experiment, fixed and immunostained for tubulin filaments by anti-alpha tubulin primary antibody and secondary antibody conjugated with the Abberrior Star Red dye. The sample was imaged with the same optical settings as the PSF characterization experiment. Given that the lifetime gradient was mostly adjacent to the ITO surface, we imaged the microtubule structure close to the basolateral cell membrane by focusing the laser at the ITO surface. When the laser is focused at the ITO and solution interface, the reflected excitation laser forms an airy disk at the conjugated focal plane on the diagnostic camera of the PicoQuant microscope. The confocal and STED lifetime image of tubulin filaments is shown in figure 3(a), where a reproducible lifetime pattern from the cell center to edge was observed among cells. The dyes on the tubulin filaments generally produced shorter lifetime at the cell lamellipodia region compared to the cell center. This suggests that as the tubulin filaments expands from the cell center to cell edge, it started from a higher position and gradually descend as it is approaching the lamellipodia at cell edge. Similar trends about cellular tubulin network have been reported in other 3D super-resolution techniques [34, 35]. The XZ scan across the cell shown in figure 3(a) also confirmed this conclusion (figure 3(b)), with fewer tubulin fibers being found at the bottom of the cell near the center. Although both the confocal and STED image revealed similar lifetime trends on the ITO surface, we noticed the lifetime

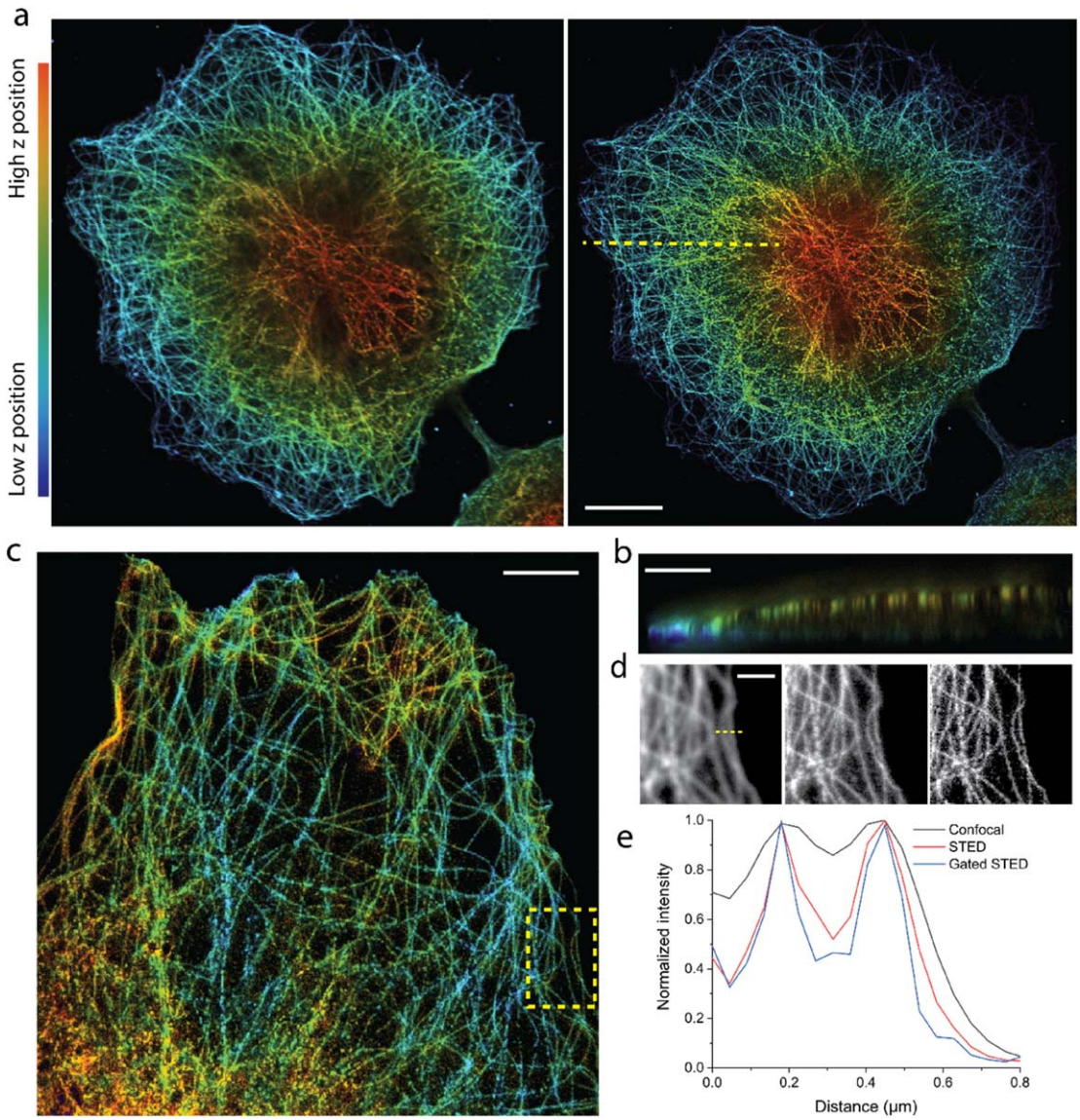

Figure 3. Lifetime based 3D-STED imaging of tubulin fibers in COS-7 cells on ITO surface. (a) a single plane XY acquisition of a confocal (left) and gated STED (right) lifetime images of the microtubules structure in the same COS-7 cells. (b) Gated STED image acquired by perform a single cross section of XZ scan at the yellow dotted line shown in panel a over the z depth of 7 μm. (c) Zoomed in XY gated STED imaging of microtubule on the ITO surface. In figures (a)–(c), the lifetime values were color coded from blue to red indicate increasing lifetime and greater distance from the ITO surface. The color is scaled independently to maximize the image contrast. (d) From left to right, confocal, STED and gated STED images of the yellow dotted line highlighted region in panel c. Scale bar = 10 μm, 3 μm, 3 μm, and 1 μm in a, b, c and d, respectively. (e) Line intensity profiles of the two tubulin fibers crossed by the single yellow dotted line in d.

contrast in the STED image was greater due to enhanced MIET effect by the STED laser. The axial contrast in the STED image not only revealed the overall descending trend of the microtubule networks at whole cell level, but also helped to differentiate the axial displacement of individual single microtubule fibers (figure 3(c)). The sharp vertical turning of the single tubulin fiber near the lamellipodia region could be detected, which was revealed by the lifetime color transition alone the fibers as shown in figure 3(c). Overall, we demonstrated that the enhanced lifetime contrast in the axial direction on the ITO surface allows for straightforward 3D-STED imaging, where the fluorophores at different z positions could be differentiated based on its lifetime values.

Lifetime gating could be applied on the ITO based 3D-STED images to further improve lateral spatial resolution as in previous gated STED [31, 36, 37]. As shown in the zoomed in region in figure 3(d), while the improvement in spatial resolution from confocal to STED image was obvious, the resolution could be further enhanced by gating the photons arrived after the STED pulse from 2.7 ns onward. This was confirmed by the full width at half maximum (FWHM) analysis of the intensity line profile across two microtubule fibers as shown in figures 3(d), (e). The gaussian fitted FWHM values to the first gaussian peak were 322 $\pm$ 6 nm, 140 $\pm$ 5 nm and 83 $\pm$ 2 nm for confocal, STED and gated STED, respectively. Also, the image contrast has improved from 0.075 for confocal to 0.316 and

0.398 for the STED and gated STED, respectively. The image contrast is defined as $(I_{max}-I_{min})/(I_{max}+I_{min})$. I_{max} and I_{min} are the intensity at the peak and valley of the two gaussian curves. As demonstrated in figure 2(b) third column, the short-lived photons were mostly located around the peripheral region of the focal point at the inner circle of the STED doughnut. Spatially, they are mixed up with the long-lived photons from the focal center that cannot be spatially filtered out by the pinhole. They blur out the image and contribute to higher background noise. Temporally, those fast photons are mostly emitted within the duration of STED pulse, which can be directly rejected out by lifetime gating [31, 36] or lifetime filtering using phasor approach based on the temporal dynamic difference of the photons emitted at the center and peripheral region of the PSF [38–40]. Remove of those fast photons could directly increase the image contrast and resolution of the STED image as previously reported. In contrast, the decrease in lifetime by the STED enhanced MIET phenomenon affects the dye lifetime decay at broader time scales, that expand well beyond the duration of STED pulse. Those photons were not fully excluded in the gated STED image. The STED images shown in figures 3(a), (c) were gated and the lifetime contrast across the cell was consistent with the MIET observed in the corresponding confocal images. This suggests that the STED enhanced MIET effect not only create greater axial contrast for easy 3D-STED image, but it can also be subjected to photon filtering to further enhance the spatial resolution.

3. General discussion and conclusion

The influence of metal and semiconductor materials to the nearby excited dye fluorescence is a complex subject of ongoing investigation. The optical and electronic properties of the material, the distance of the dye to the material interface, and the presence of plasmonic resonance can all influence the light emitting process of the dyes in proximity [12, 41, 42]. At less than 5 nm distance, the nonradiative energy transfer to the metal surface is the dominant process and it substantially reduces the probability of photon emission. At a longer distance beyond the quenching layer, greater number of photons can be emitted for a given time due to accelerated lifetime decay rate near the metal surface. Spending less time in the excited state also reduces the probability of triplet state induced photobleaching which increases total number of photons emitted [12, 41]. When the excitation light becomes locally trapped near the metal surface due to plasmonic resonance coupling, such as in nanoantenna, the apparent brightness and lifetime decay rate of the dyes could be increased substantially [27, 43, 44]. In the current study, we focus on the lifetime aspect of the light emission process near the ITO surface. Namely, the MIET effect, in which electromagnetic waves from the oscillating dipole of an excited fluorophores are coupled to the surface plasmon of the semiconductor. Inside the semiconductor, both the abundance and mobility of the free charge carriers influences the efficiency and range distance of the MIET effect [16, 45]. In the case of ITO, Tin doping increases the abundance of the free electron. In presence of the STED laser, the electromagnetic energy from the STED laser could be coupled to the surface plasmons of ITO causing increased mobility of the free electrons. The motion of the resonating electrons could deviate beyond the physical barrier of the ITO surface like in nanoantenna to enhance resonance coupling with nearby fluorophores [46]. In current study, both the magnitude and distant range of the MIET effect near the ITO surface were enhanced by the STED laser.

The STED laser enhanced MIET effect affects the dye lifetime decay beyond the STED laser pulse, which is distinct from the STED laser effect alone [6, 30]. Through PSF characterization, we show that the reduction of lifetime was amplified close to the ITO interface. Spatially, the lifetime reduction by MIET effect extended from the surrounding STED doughnut into the focal center, possibly due to longitudinal traveling of the SPR wave along the ITO surface. Those photons are permitted at the pinhole position that sufficiently collected by the detector. Vertically, a sharp gradient of lifetime was extended for up to 400 nm from the ITO surface. We show that this lifetime gradient is sufficient to introduce lifetime based axial contrast for 3D-STED imaging inside cells. It was sensitive enough to reveal the vertical displacement of single tubulin fibers in the cell. Based on the PSF analysis, we suggest the STED enhanced MIET affect the fluorophores located $<$400 nm from the ITO surface. At increased distance from the ITO surface, the lifetime contrast will eventually diminish. One other practical limitation is that increase of STED laser power beyond 20 mW could cause damage to the ITO coating, we found that $\sim$12 mW STED laser power produced optimal result in our setup.

On the glass substrate, a slight lifetime contrast was observed for photons emitted from the focal plane and above as shown in figure 2. This is due to incomplete fluorescence depletion at the inner circle of the STED doughnut, and this effect is most intense at the focal plane and weakens as it moves away from the focal plane. However, those fast photons are spatially located at the peripheral ring at the conjugated focal plane at the pinhole position that are partially rejected. In addition, those fast photons can be temporally filtered out by lifetime gating. The MIET modulated photons from ITO surface on the other hand are spatially centered and long lived, which can survive the pinhole filtering and lifetime gating. Nevertheless, careful alignment of the STED depletion beam should be performed to avoid asymmetrical depletion of the STED beam in the vertical direction. The pinhole

position should also be centralized to avoid biased detection of those STED laser affected fast photons.

In conclusion, we showed that by performing standard STED imaging on the ITO coated coverslip, a vertical lifetime gradient adjacent to the ITO surface was produced that could be used to introduce the axial contrast for 3D-STED imaging. The range of the lifetime gradient covers up to 400 nm that is suitable for 3D imaging of cellular structures. We showed that the axial contrast was sensitive enough to distinguish axial displacement of single tubulin fibers. The great advantage of current 3D-STED approach is its simplicity, given that most STED microscope are capable of lifetime measurement, no additional optical modification is required. In addition, the sample preparation procedure is standard, and the ITO coverslips are commercially available. Therefore, we anticipate broad adaptation of this method by the super-resolution imaging community.

4. Method and materials

4.1. Sample preparation

The ITO coated glass coverslip (06489-AB, SPI supplies, PA, USA) were commercially manufactured by depositing 750 nm ITO onto 170 μm thick glass coverslip that produce 8–12 Ω electric resistance according to the manufacture. The Ω value is indicative of the ITO thickness with the ITO coating thickness inversely proportional to electric resistance. Prior to placing samples on top, the ITO coverslip was plasma cleaned for 3 min and washed by 70% Ethanol. For the bead imaging experiments, the 430 nm purple polystyrene beads (VFP-0562–5 Spherotech) used were sonicated for a few second to reduce bead clustering. COS-7 cells (ATCC CRL-1651) were placed on either glass or ITO coated coverslip in 6 well plate 18 h prior to the imaging experiment. The cells were cultured in DMEM supplemented with 10% Fetal Bovine Serum (FBS) at 37 °C and 5% CO_2 incubator. For immunofluorescence imaging, the cells were fixed in 4% paraformaldehyde for 10 min, and permeabilized by 0.02% Triton X-100 for 5 min at room temperature. The permeabilized cells were washed and incubated in 5% bovine serum albumin BSA for 30 min to prevent non-specific antibody binding. 2 ul of anti-alpha tubulin antibody (ab216650, Abcam) was added to the sample at 1:1000 dilution factor and incubated at room temperature for 1 h. The sample was washed and stained with Abberior STAR RED conjugated goat anti rabbit secondary antibody (STRED-1002-500UG, Abberior, Göttingen, Germany) for another 30 min prior to washing and imaging in PBS buffer.

4.2. Optical setup

The STED image acquisition was conducted on the PicoQuant MicroTime 200 STED microscope (PicoQuant GmbH, Berlin, Germany) equipped with a FLIM bee galvanometer scanner (PicoQuant GmbH, Berlin, Germany). A 640 nm picosecond pulsed laser (LDH series, PicoQuant GmbH, Berlin, Germany) was used for the excitation. A 765 nm pulsed STED laser (VISIR-STED, PicoQuant GmbH, Berlin, Germany) was used for stimulated depletion. The STED pulse was stretched to ∼300 ps to avoid two-photon excitation and reduce photobleaching. All lasers were set to pulse at 40 Mhz with the STED laser pulse electronically adjusted to arrive at ∼200 ps delay from the excitation laser. This laser configuration provided the maximal depletion efficiency for the dyes used. The two lasers were reflected to the objective by a 640/760 nm dichroic mirror (Chroma, Bellows Falls, VT). Samples were imaged through either a 60X Water immersion objective (NA 1.30, UplanSApo, Olympus, Tokyo, Japan) or a 100X Oil immersion objective (NA1.40, UPlanSApo, Olympus, Tokyo, Japan) as specified in the text. On the PicoQuant STED system, the easy STED approach [47] was used to generate the doughnut STED depletion pattern. Here, a chromatic sensitive segmented wave plate was placed in the back of the 100X Oil objective. Due to the wavelength sensitive nature of the birefringent material used in the waveplate, the 640 nm laser was retarded by a whole wavelength that forms a normal diffraction limited spot at the focal point, while the STED laser was retarded by a half wavelength to form a doughnut pattern at the focal point with zero intensity in the center [47]. The fluorescence emitted was collected by the same objective and spatially filtered by a 100 μm pinhole at the conjugated focal plane. The light passing through the pinhole was guided and focused onto the Single Photon Avalanche Diodes (SPAD) (SPCM AQRH-14 TR, Excelitas Technologies, Waltham, MA). A 690/70 band pass filter (Chroma, Bellows Falls, VT) was inserted in front of a SPAD detector to clean up the reflected excitation laser, the STED laser and the stimulate emissions from the dyes.

To build up the lifetime histogram, the photons arrival times were registered in Time-Correlated Single Photon Counting TCSPC format using a Hydraharp 400 (PicoQuant GmbH, Berlin, Germany). The image acquisition and data analysis were performed using the SymPho Time 64 (PicoQuant GmbH, Berlin, Germany). The STED images were raster-scanned in frame-by-frame cumulative mode with total pixel dwell time of ∼1 ms. For low resolution beads lifetime image in figure 1, an area of 80 μm^2 was scanned in a 256 × 256-pixel array and pixel size of 300 nm. For high resolution image in figures 2 and 3, pixel sizes were set to 80 nm and 20 nm respectively for confocal and STED acquisition. For XZ STED imaging in figure 2, a 1200 × 2300 nm^2 rectangle area in XZ plane across the center of a single bead was scanned with pixel size of 20 nm.

4.3. FLIM analysis

Two images were generated from the PicoQuant STED microscope, one was the intensity image, the other was the Fast FLIM image. The pixel value in the intensity image was the accumulated photon number over the pixel dwell time. The pixel value in the Fast FLIM was the average photon arrival time of the given pixel location. For image display, the Fast FLIM image was often weighted by the pixel intensity values. This was achieved by mapping the intensity weighted FLIM image to another 1024×1024 colormap image. There were two gradients across the horizontal and vertical axis of the colormap image. The horizontal index of the image was color coded from blue to red to indicate the pixel lifetime value, and the vertical index of increasing brightness from top to bottom to report the pixel intensity value. The pixel intensity value in the intensity image determines the column index and the value in the Fast FLIM value determines the row index of the reconstructed intensity weighted FLIM image. The non-intensity weighted raw Fast FLIM image could reveal lifetime distribution of low light conditions. However, the Fast FLIM image contained high noise levels from the background. To increase the signal to noise ratio of the Fast FLIM image, we restricted the intensity weighting of the Fast FLIM image by 1% of the maximal intensity value of the intensity image. In addition, a lowess smoothing was applied to the Fast FLIM image to increase the signal to noise ratio.

To quantify the STED enhanced MIET effect on the ITO surface in figure 2, the dye lifetime was tail fitted to single exponential decay model in the gated lifetime window of 2.7 ns to 25 ns. The single exponential model used was $I = Amp_{*} \exp(-t/\tau) + background$. Amp is the amplitude of the lifetime, and the τ is the lifetime modeled.

Acknowledgments

YM acknowledges the Earlier Career Fellowship funding from the National Health and Medical Research Council of Australia (APP1139003). We thank the Katharina Gaus Light Microscopy Facility at the University of New South Wales for providing trainings on the microscope and technical support. Especially thank to Dr Michael Carnell for helpful discussions on the results.

Data availability statement

The data that support the findings of this study are available upon reasonable request from the authors.

Author contributions

Conceptualization, investigation, Y.M.; writing, review and editing, Y.M., A.M and Y.Y. methodology, data curation, analysis, Y.M. A.M. and Y.Y.; supervision, project administration, Y.M, K.G.; All authors have read and agreed to the published version of the manuscript.

Conflict of interest statement

The authors declare no competing financial interest.

ORCID iDs

Yuanqing Ma https://orcid.org/0000-0003-0557-4559

References

[1] Wilson T and Sheppard C 1984 *Theory and Practice of Scanning Optical Microscopy* 180 (London: Academic)
[2] Hell S W and Wichmann J 1994 Breaking the diffraction resolution limit by stimulated emission: stimulated-emission-depletion fluorescence microscopy *Opt. Lett.* **19** 780–2
[3] Klar T A *et al* 2000 Fluorescence microscopy with diffraction resolution barrier broken by stimulated emission *Proc. Natl Acad. Sci.* **97** 8206–10
[4] Pereira A *et al* 2019 Coherent-hybrid STED: high contrast sub-diffraction imaging using a bi-vortex depletion beam *Opt. Express* **27** 8092–111
[5] Schmidt R *et al* 2008 Spherical nanosized focal spot unravels the interior of cells *Nat. Methods* **5** 539–44
[6] Auksorius E *et al* 2008 Stimulated emission depletion microscopy with a supercontinuum source and fluorescence lifetime imaging *Opt. Lett.* **33** 113–5
[7] Han K Y and Ha T 2015 Dual-color three-dimensional STED microscopy with a single high-repetition-rate laser *Opt. Lett.* **40** 2653–6
[8] Hein B, Willig K I and Hell S W 2008 Stimulated emission depletion (STED) nanoscopy of a fluorescent protein-labeled organelle inside a living cell *Proc. Natl Acad. Sci.* **105** 14271–6
[9] Osseforth C *et al* 2014 Simultaneous dual-color 3D STED microscopy *Opt. Express* **22** 7028–39
[10] Antonello J *et al* 2016 Coma aberrations in combined two- and three-dimensional STED nanoscopy *Opt. Lett.* **41** 3631–4
[11] Patton B R *et al* 2016 Three-dimensional STED microscopy of aberrating tissue using dual adaptive optics *Opt. Express* **24** 8862–76
[12] Enderlein J 2000 A theoretical investigation of single-molecule fluorescence detection on thin metallic layers *Biophys. J.* **78** 2151–8
[13] Sahoo H 2011 Förster resonance energy transfer—A spectroscopic nanoruler: Principle and applications *J. Photochem. Photobiol., C* **12** 20–30
[14] Chizhik A I *et al* 2014 Metal-induced energy transfer for live cell nanoscopy *Nat. Photonics* **8** 124–7
[15] Oleksiievets N *et al* 2020 Wide-field fluorescence lifetime imaging of single molecules *The Journal of Physical Chemistry A* **124** 3494–500
[16] Ghosh A *et al* 2019 Graphene-based metal-induced energy transfer for sub-nanometre optical localization *Nat. Photonics* **13** 860–5
[17] Moerland R J and Hoogenboom J P 2016 Subnanometer-accuracy optical distance ruler based on fluorescence quenching by transparent conductors *Optica* **3** 112–7

[18] Benda A et al 2006 Fluorescence lifetime correlation spectroscopy combined with lifetime tuning: new perspectives in supported phospholipid bilayer research *Langmuir* **22** 9580–5
[19] Axelevitch A, Gorenstein B and Golan G 2012 Investigation of optical transmission in thin metal films *Phys. Proc.* **32** 1–13
[20] Kim H et al 1999 Electrical, optical, and structural properties of indium–tin–oxide thin films for organic light-emitting devices *J. Appl. Phys.* **86** 6451–61
[21] Cao W et al 2014 Transparent electrodes for organic optoelectronic devices: a review *Journal of Photonics for Energy* **4** 040990
[22] Chen Z et al 2013 Fabrication of highly transparent and conductive indium–tin oxide thin films with a high figure of merit via solution processing *Langmuir* **29** 13836–42
[23] Nicovich P R et al 2018 Characterization of functionalized glass and indium tin oxide surfaces as substrates for super-resolution microscopy *J. Phys. D* **52** 034003
[24] Fan S et al 2019 Observing the reversible single molecule electrochemistry of alexa fluor 647 dyes by total internal reflection fluorescence microscopy *Angew. Chem. Int. Ed.* **58** 14495–8
[25] Rhodes C et al 2006 Surface plasmon resonance in conducting metal oxides *J. Appl. Phys.* **100** 054905
[26] Kanehara M et al 2009 Indium tin oxide nanoparticles with compositionally tunable surface plasmon resonance frequencies in the near-ir region *J. Am. Chem. Soc.* **131** 17736–7
[27] Bakker R M et al 2008 Nanoantenna array-induced fluorescence enhancement and reduced lifetimes *New J. Phys.* **10** 125022
[28] Brewer S H and Franzen S 2002 Indium tin oxide plasma frequency dependence on sheet resistance and surface adlayers determined by reflectance FTIR spectroscopy *J. Phys. Chem. B* **106** 12986–92
[29] Galiani S et al 2012 Strategies to maximize the performance of a STED microscope *Opt. Express* **20** 7362–74
[30] Lin P-Y et al 2013 Fluorescence lifetime imaging microscopy with subdiffraction-limited resolution *Jpn. J. Appl. Phys.* **52** 028004
[31] Vicidomini G et al 2011 Sharper low-power STED nanoscopy by time gating *Nat. Methods* **8** 571–3
[32] Sonnefraud Y et al 2014 Experimental proof of concept of nanoparticle-assisted STED *Nano Lett.* **14** 4449–53
[33] Urban N T et al 2018 Nanoparticle-assisted STED nanoscopy with gold nanospheres *ACS Photonics* **5** 2574–83
[34] Olivier N et al 2013 Resolution doubling in 3D-STORM imaging through improved buffers *PLoS One* **8** e69004–69004
[35] Dugina V et al 2016 Interaction of microtubules with the actin cytoskeleton via cross-talk of EB1-containing +TIPs and γ-actin in epithelial cells *Oncotarget* **7** 72699–715
[36] Vicidomini G et al 2013 STED nanoscopy with time-gated detection: theoretical and experimental aspects *PLoS One* **8** e54421
[37] Moffitt J R, Osseforth C and Michaelis J 2011 Time-gating improves the spatial resolution of STED microscopy *Opt. Express* **19** 4242–54
[38] Wang L et al 2018 Resolution improvement in STED super-resolution microscopy at low power using a phasor plot approach *Nanoscale* **10** 16252–60
[39] Tortarolo G et al 2019 Photon-separation to enhance the spatial resolution of pulsed STED microscopy *Nanoscale* **11** 1754–61
[40] Lanzanò L et al 2015 Encoding and decoding spatio-temporal information for super-resolution microscopy *Nat. Commun.* **6** 6701
[41] Stefani F D et al 2005 Surface-plasmon-mediated single-molecule fluorescence through a thin metallic film *Phys. Rev. Lett.* **94** 023005
[42] Naik G V, Shalaev V M and Boltasseva A 2013 Alternative plasmonic materials: beyond gold and silver *Adv. Mater.* **25** 3264–94
[43] Punj D et al 2013 A plasmonic 'antenna-in-box' platform for enhanced single-molecule analysis at micromolar concentrations *Nat. Nanotechnol.* **8** 512–6
[44] Kinkhabwala A et al 2009 Large single-molecule fluorescence enhancements produced by a bowtie nanoantenna *Nat. Photonics* **3** 654–7
[45] Ghosh A et al 2021 Graphene- and metal-induced energy transfer for single-molecule imaging and live-cell nanoscopy with (sub)-nanometer axial resolution *Nat. Protoc.* **16** 3695–715
[46] Koenderink A F 2017 Single-photon nanoantennas *ACS Photonics* **4** 710–22
[47] Reuss M, Engelhardt J and Hell S W 2010 Birefringent device converts a standard scanning microscope into a STED microscope that also maps molecular orientation *Opt. Express* **18** 1049–58